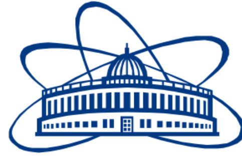

JOINT INSTITUTE FOR NUCLEAR RESEARCH
Dzhelepov Laboratory of Nuclear Problems
Scientific-Experimental Division of Colliding Beams

FINAL REPORT ON THE
SUMMER STUDENT PROGRAM

“Study of some effects induced by 20 MeV electrons irradiation on GaAs:Cr detector using Raman Spectroscopy”

Student:
Daina Leyva Pernía.
Higher Institute of Sciences and Applied Technologies, Havana University, Cuba
d.leyvapernia02@gmail.com

Supervisor:
Dr. Antonio Leyva Fabelo

Participation period:
July 10th - August 31st

Dubna, 2018

Abstract.

The use of GaAs:Cr semiconducting detectors has increased in recent years due to its recognized resistance to the radiation damage, good charge carrier transport properties, high effective Z, relative low production cost, etc. The study of radiation effects on the GaAs:Cr is highly important because it gives scientists the possibility to better understand how radiation affects the material and its properties, to elaborate strategies to preserve them, and even to give the possibility to use these radiations in order to improve the detector and material characteristics. The aim of this work, carried out in the frames of the JINR Summer Student Program - 2018, was to provide some knowledge in the topic of the electrons radiation effect on GaAs:Cr detector using Raman spectroscopy and other available methodologies. With this objective, a GaAs:Cr detector was irradiated with 20 MeV electrons on the LINAC-800 accelerator and measured its CCE and Raman spectra in incident and exit surfaces before and after irradiation. After irradiation, an increment in collection efficiency was observed. The Raman spectra measured before and after the irradiation showed significant differences for the observed behaviors in both analyzed surfaces. The effect of the electrons on the incident surface was strong and appears to be associated with the marked changes in the free carrier concentration and the slightly modification of the tensional state of the structure, stimulated by the irradiation. On the opposite side the effects were significantly lesser. Additionally, using the mathematical simulation was calculated the deposited energy and the displacement per atom distributions inside the irradiated detector for the used energy in two geometrical configurations. Employing a very simple image processing was estimated the fluence in the target sample from the obtained image of the beam spot. Finally, the sensitive effective depth in the Raman measurements was calculated. The evaluation of the obtained results continues and some recommendations for the future development of the research and the improvement of the analyzes are presented in the text.

Table of contents.

	Contents	Page
I.	Introduction.	4
II.	Estimation of the electron fluence in the irradiated target.	5
III	Calculation of the Raman Spectroscopy effective sensitive depth in GaAs detector.	6
IV	Simulation by Monte Carlo of electron deposited energy distribution in the irradiated sample.	7
V	Evaluation of the radiation damage in *dpa* terms in GaAs:Cr sample using the MCCM code system.	8
VI	Measurement of CCE in GaAs:Cr before and after irradiation.	10
VII	Measurement of the Raman spectra for pristine and irradiated GaAs:Cr sample.	12
VIII	Analysis of the measured Raman spectra.	15
IX	Acknowledgments.	18
X	References.	19

Introduction.

The use of GaAs:Cr semiconducting detectors has increased vastly in recent years. Their characteristics allow to have a large energy lost in short distance, a very good energy resolution, and comparing to silicon and other semiconducting detectors it has been proved that they are more resistant to radiation, which makes them great for extreme radioactive environments [1].
The study of radiation effects on the GaAs:Cr is highly important because it gives scientists the possibility to have a better understanding on how radiation affects the material and its properties, to elaborate strategies to preserve them, and gives the possibility of using radiation to improve the detector and material characteristics.
The main objective of this work, carried out in the frames of the JINR Summer Student Program - 2018, is to provide a bit of knowledge in this broad topic related to the effect of radiation on semiconductors, specifically in our case in the GaAs:Cr detector, using Raman spectroscopy and other available methodologies in the JINR.
In figure 1 are shown the photos of a high resistivity GaAs:Cr detector employed in our experiment. This is a 300 μm detector with 4.5 x 4.5 mm^2 area.
As represented in figure 1(a), the irradiation took place on the surface (input) where the detector has a metal square electrode (Ni anode). On the output surface the electrode covers irregularly the half of the surface (Ni cathode) (figure 1(b)).

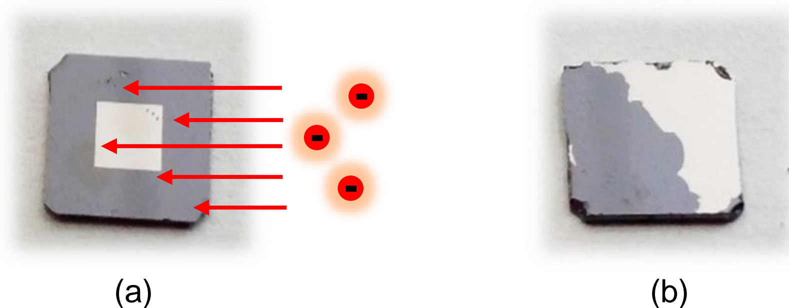

(a) (b)

Figure 1. Photos of the GaAs:Cr target sample surfaces: the input or exposed to radiation (a), and the exit or opposited to radiation (b).

The detector was irradiated with 20 MeV electrons on the LINAC-800 accelerator from the Dzhelepov Laboratory of Nuclear Problems (DLPN), in figure 2. The electron beam characteristics are: energy of the electrons E_{e-} = 20 MeV, intensity of the current I = 10 mA, frequency f = 10 Hz, pulse length Δt = 1.5 μs, total irradiation time T_{irrad} = 30 min.

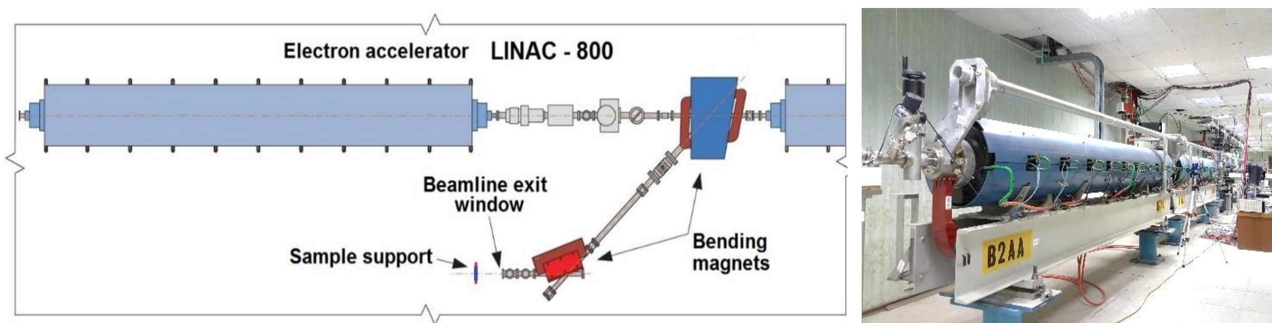

Figure 2. Schematic representation of the LINAC-800 accelerator (left), and its panoramic photo (right).

Raman Spectroscopy was employed to obtain information about the changes in the material exposed to the irradiation. This method allows to observe vibrational, rotational, and other low-frequency modes in a system [2].
The Raman measurements were made on the zones of the input and exit detector surfaces where there are no electrodes. The measurements were done at room temperature using a spectrometer, model CARS-Solar TI, shown in figure 3. As source of excitation a He-Ne laser (632.8 nm) was used. The following conditions were applied: diffraction grid of 1200 lines/mm, objective 40x and acquisition time 70 s.

Figure 3. Raman Spectrometer CARS-Solar TII.

Some techniques and methodologies additionally used in the work are mentioned and explained in the text.

Estimation of the electron fluence in the irradiated target.

The GaAs:Cr detector was irradiated under a flux of 20 MeV electrons. The total amount of electrons (e^{-}) that impact all the exposed surface (target detector + its holder + control luminescent screen) is known to be 1.685×10^{15} e^{-}. This value was calculated from the know data of the beam.
The figure 4 is a photo taken in real time during irradiation. The detector (dark circle) is surrounded by a white halo which is the luminescent emission of the detector’s holder made with PCB and the luminescent screen where they were placed.

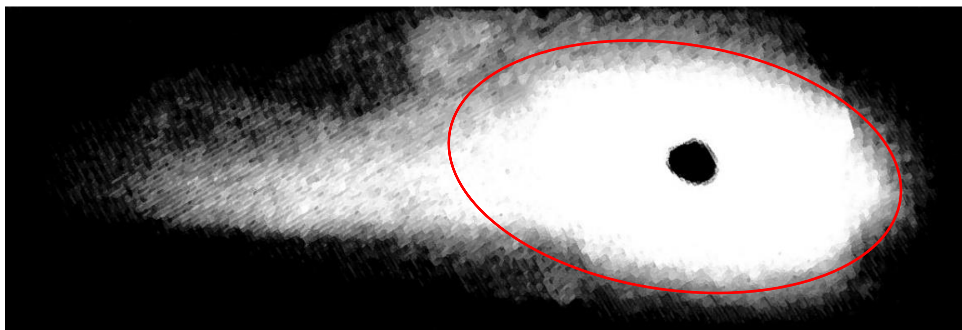

Figure 4. Beam spot in the arrangement consisting of the target detector, the detector’s holder and luminescent screen. The red line represents the ellipsis used for the calculation.

Starting from the rough approximation that exists an area on the image with an elliptic shape (marked in red on figure 4) where all the flux of e^{-} that impact the target is concentrated homogenously, the simple software ImageJ [3] was used to calculate approximately this

area on terms of number of pixels (A_T). The area of the black spot that represents the detector (A_D) was also calculated.
With this information can established the following relation (equation 1).

$$\frac{A_T}{A_D} = \frac{N_T}{N_D}, \quad (1)$$

where N_T and N_D represent the number of electrons that impact on the areas A_T and A_D respectively. As was mentioned above, N_T is assumed to be 1.685×10^{15} e$^-$.
The result was $N_D = 6.21148 \times 10^{13}$ e$^-$.
The fluence of radiation over the detector (ϕ_D) can be calculated dividing N_D by the known real area of the detector $A_{RD} = 1.25664 \times 10^{-1}\ cm^2$.
The obtained fluence was $\boldsymbol{\phi_D = 4.94294 \times 10^{14}\ e^-/cm^2}$.
Using the same procedure but this time the contour of the areas was taken in a drawn by hand figure instead of an ellipse to guarantee a more accurate result, the obtained fluence was $\boldsymbol{\phi_D = 2.85384 \times 10^{14}\ e^-/cm^2}$.
A third and more accurate method to calculate fluence was based on image processing of the beam spot (figure 4) using the code systems Photoshop [4] and Matlab [5].
First the image was converted to a gray scale to be processed and transformed into a matrix pixel by pixel.
This matrix will contain numbers from 0 to 1, where 0 corresponds to black color and zero exposure. The value 1 corresponds to lightest pixels and it is related to maximum exposure.
Then, assuming that the exposition of the detector surface was equal to the values in its surrounding area, where the spot is brighter and more homogeneous, the image of figure 4 was modified turning the black spot into a light area with brightness values similar to the adjacent ones. From this new image it was obtained a second matrix, with the same dimensions of the first one.
Subtracting both matrixes was obtained a third one which only shows approximately how much radiation was received by the detector in terms of luminosity.
Assuming that all the electrons (1.685×10^{15} e$^-$) corresponds to the total luminosity represented by the second matrix and establishing a corresponding proportionality with the third matrix it was possible to estimate that in the zone of the detector the number of impacting electrons is 2.2372×10^{13} e$^-$.
To calculate the fluence in the target sample was divided this value by the detector area resulting in a fluence $\boldsymbol{\phi = 1.8643 \times 10^{14}\ e^-/cm^2}$. This value is a bit smaller than the obtained by first method but on the same order of magnitude and little more precision.

Calculation of the Raman Spectroscopy effective sensitive depth in GaAs detector.

To obtain the Raman spectra of the detector, both before and after irradiation, it was used He-Ne laser ($\lambda = 632.8\ nm$). For any analysis of the measured Raman spectra, it is very important to know what is the sensitive depth of the method, or the analysis effective depth in the target material, in this case the GaAs:Cr semiconductor.
The penetration depth (δ_e) is a measure of how deep any electromagnetic radiation can penetrate into a material. It is defined as the depth at which the electromagnetic field of the wave inside the material falls to $1/e$ (about 37 %) of its original value at the surface and thereby the intensity of the wave has decreased to $1/e^2$, or about 13% of its surface value.

According to Beer-Lambert law, the intensity of an electromagnetic wave inside a material falls off exponentially from the surface as shown in equation 2.

$$I = I_0 e^{-\alpha z} \qquad (2)$$

where I and I_0 stand for the intensity of the electromagnetic wave inside the material and in its surface respectively, α is the attenuation coefficient of the material and z is the depth inside the material.
The effective penetration depth can be obtained from equation 2 and calculated by the expression in equation 3.

$$\delta_e = \frac{2}{\alpha}, \qquad (3)$$

The attenuation constant for an electromagnetic wave at normal incidence of radiation on a material is also proportional to the imaginary part of the material's refractive index n. This relation can be written as in equation 4.

$$\frac{\alpha}{2} = \frac{1}{\delta_e} = \frac{\omega}{c} Im\big(\eta(\omega)\big) = \frac{2\pi}{\lambda} Im\big(\eta(\omega)\big) = \frac{2\pi}{\lambda} k \qquad (4)$$

where η denotes the complex index of refraction, ω is the frequency of the radiation, c is the speed of light in vacuum and λ is the wavelength of the radiation, k, the imaginary part of the refractive index, is called the extinction coefficient and indicates the amount of attenuation when the electromagnetic wave propagates through the material [6] .
Then, the penetration depth of laser radiation with $\lambda = 632.8$ nm and hence the effective depth of analysis by Raman spectroscopy (d), may be determined from the relation shown in equation 5.

$$d = \frac{\lambda}{2\pi k} \qquad (5)$$

Correspondingly, in case of the GaAs:Cr system the depth of analysis is $\boldsymbol{d \sim 507.8\ nm}$.

Simulation by Monte Carlo of electron deposited energy distribution in the irradiated sample.

As a complementary result, the deposited electron energy distribution was obtained.
Firstly was modeled the detector under the incidence of 20 MeV electrons using the MCNPX code, and secondly was added to the geometry the detector’s PCB holder (figures 5 (a) and (b) respectively) for comparison.
The two images have the blue area representing the active area of the detector, made of GaAs:Cr. In yellow the anode and cathode, both made of nickel. In gray the PCB holder. The arrows show the 20 MeV electron direction.

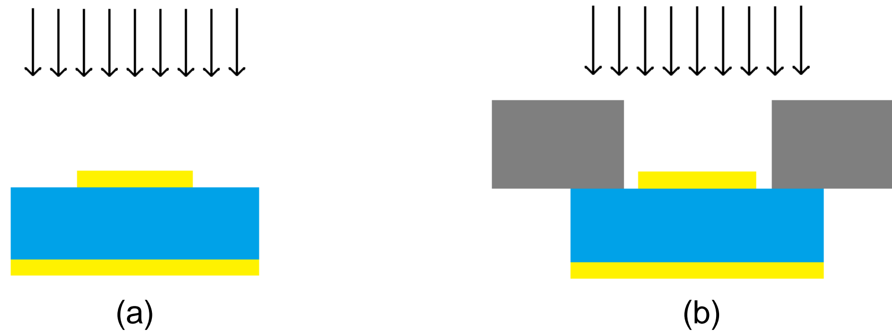

Figure 5. The experimental geometry modeled without PCB (a) and considered the PCB holder (b).

The results of our modeling are shown in the next graph (figure 6).

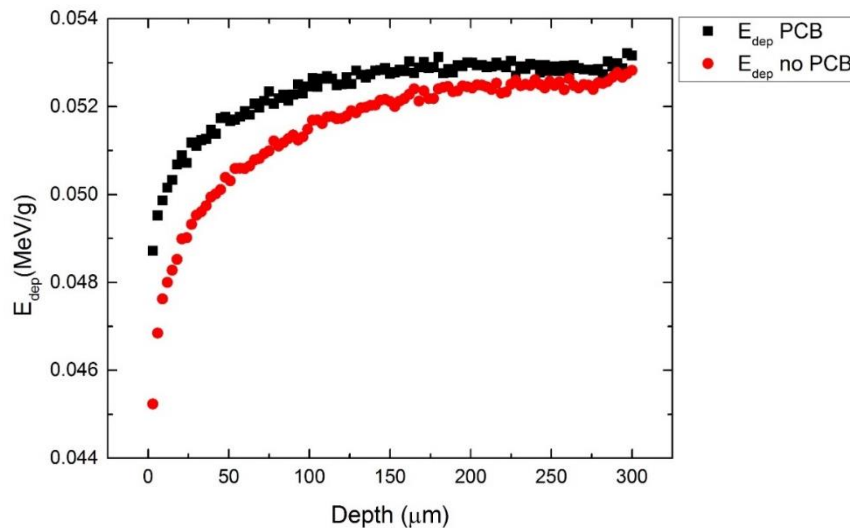

Figure 6. In-depth total energy deposition by the incident electrons inside the detector.

As can be seen, the behavior of the deposited energy with the depth is monotonously increasing until half the material, and starting from 150 μm this behavior is significantly attenuated.
For the case where the presence of the PCB is considered, the results were slightly higher in the entire depth range of the GaAs:Cr. This behavior may be the result of a greater energy deposition caused by the increment of the interaction probability in the target material as a consequence of the primarily electron interaction in the PCB.

Evaluation of the radiation damage in dpa terms in GaAs:Cr sample using the MCCM code system.

Along with the electron deposited energy distribution, it was also obtained from the Monte Carlo simulation the energy flux distribution inside the target. This information was introduced into the MCCM code system [7] which calculates the number of displacements

per atom (N_{dpa}) for each emitted particle. This program also calculates the displacement cross section for electrons and positrons for every material atom ($\sigma_{dpa}^{e-, e+}$).
Once again, the first sample run was a model of our detector directly under the incidence of 20 MeV electrons (like figure 5(a)), and on the second sample it was also considered the PCB holder (figure 5(b)).
In figures 7 and 8 it is shown the *dpa* cross section for e^- and e^+ respectively in GaAs:Cr.

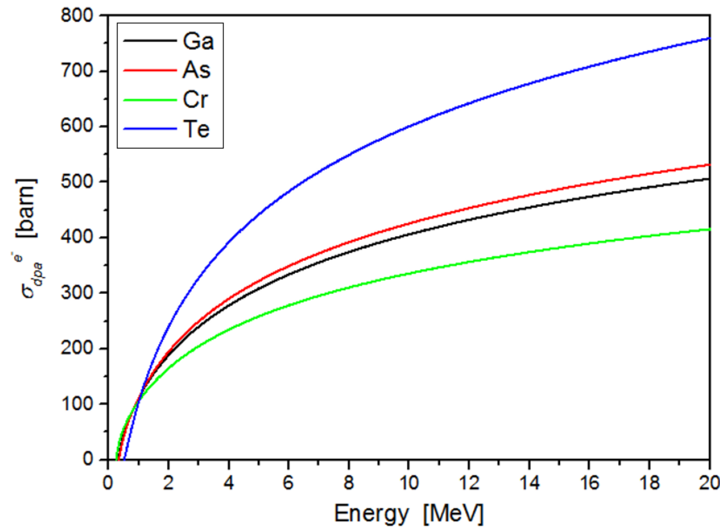

Figure 7. Displacement cross section with the electron energy behavior in GaAs:Cr.

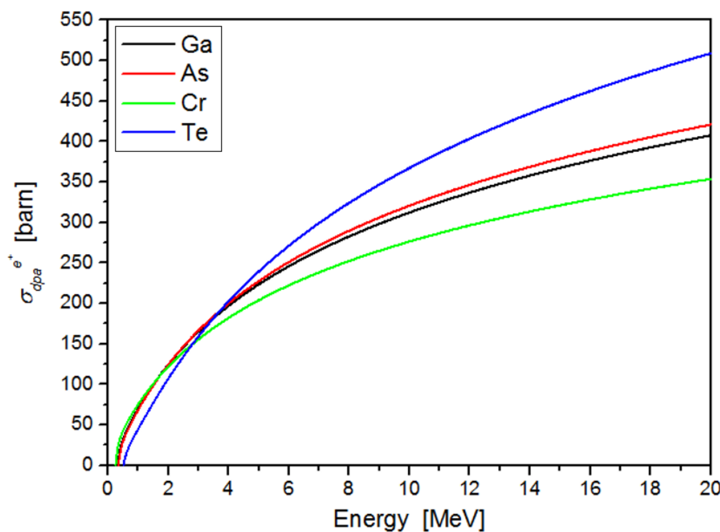

Figure 8. Displacement cross section with the positron energy behavior in GaAs:Cr.

These distributions are indispensable for the calculation of the atomic displacements. It also allows to determine the threshold energies required for the occurrence of atomic displacements in the material according to the target atom, as well as the energy of the incident particle required for the processes of displacement cascades to be probable [7].
The results of the modeling, both considering and not considering PCB holder, are shown on the next graph (figure 9).

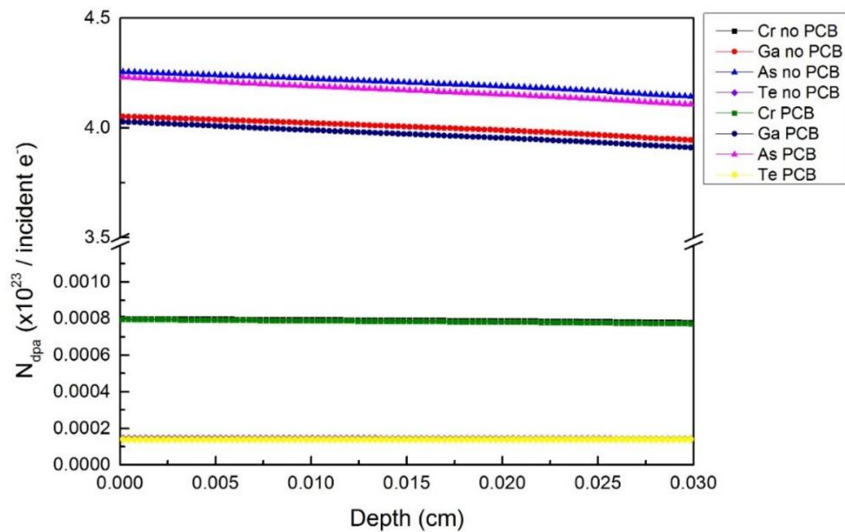

Figure 9. In-depth total N_{dpa} distribution for each atom species of the GaAs:Cr for both analyzed geometries.

As can be seen, for Ga and As the N_{dpa} are slightly higher if the PCB holder is not considered. For Cr and Te this difference is imperceptible. In general, the behavior of the N_{dpa} is slightly decreasing for each kind of atom.

Measurement of CCE in GaAs:Cr before and after irradiation.

The charge collection efficiency (CCE) provides information about how effective is the detector collecting charge carriers. The CCE was determined by results of measurements made on the installation shown in figure 10.

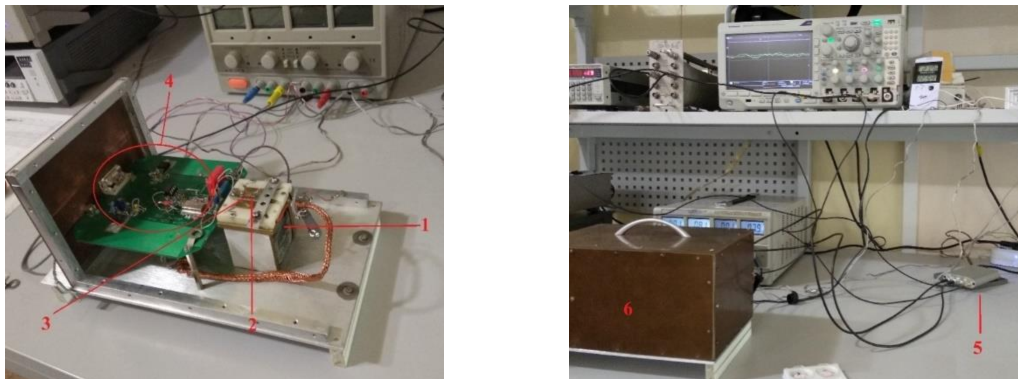

Figure 10. The measurement installation: (1) Sr-90 source, (2) detector, (3) contact needle, (4) amplifying and processing electronics, (5) ADC, and (6) metal box container.

In this installation the e^- from Sr-90 source (placed inside a Pb shielding) are collimated and pass through the detector producing ionization. The generated carriers are transported by the electric field and the induced signal is collected by a metal needle, conducting it to the electronic devices that process, amplify and convert it. The metal box container has on the inner side of the top a trigger that works with 2 scintillators.
In figure 11 is shown a scheme of the measurement setup.

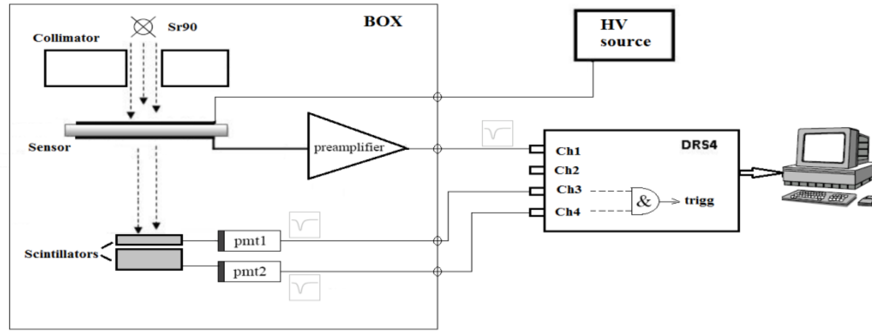

Figure 11. Schematic representation of the CCE measurement setup, explained above.

With this installation was measured the response to the charge generated by ionization inside the detector plus the background noise from the chain of electronic devices that read and translate the signal.
The signal and the pedestal are characterized by different probability distributions. Pedestal, as random background noise, can be fitted to a Gaussian distribution. Its value defines the baseline of the real signal and its width the noise from the readout chain. The signal from the detector has a Landau distribution, with a much slower decline.
The values of s (signal), p (pedestal) and σ (standard deviation of Landau distribution) were measured before and after irradiation. The measurements were taken before irradiation at 23.7 ºC and after irradiation at 21.7 ºC. The applied voltage was -200 V.
With this information it was possible to obtain the relative CCE^* (equation 6).

$$CCE^* = \frac{(s-p)}{(s_0-p_0)} \quad , \qquad (6)$$

where s, p and s_0, p_0 are the signal and pedestal after and before irradiation respectively. The results are shown in Table 1.

Table 1. Measurements of s, p, σ.

Parameter	Before irradiation	After irradiation
s	5.65	6.69
p	2.82	2.52
σ	3.38	2.96

A value of CCE^* = 1.47 was obtained.

This result shows an increasement of the charge collection efficiency after irradiation which can be related to the change in the free carrier density induced by irradiation explained below when the Raman spectra is analyzed.
Nevertheless, it is expected for this detector to have a small efficiency because electrodes are damaged (see photos below), so the electric field inside the detector should be very irregular and most charge carriers may be loss. By overlapping the images of the detector sides, as is presented in figure 12, it can be seen that the area where the anode and the cathode geometrically coincide is really small.

(a) (b) (c)

Figure 12. Photos of the studied detector: (a) input surface with the Ni anode (square shaped with light color), (b) exit surface with the cathode (irregular shape covering less than the half of the detector surface, light color), and (c) superposition of both images for comparison.

Measurement of the Raman spectra for pristine and irradiated GaAs:Cr sample.

The spectra of the two sides of the studied target before irradiation are presented in figure 13. From the superposition of them can be observed some important differences.
In both Raman spectra we can see the presence at $\sim 292\ cm^{-1}$ the longitudinal optical (LO) Ga-As phonon mode, which agrees with the experimental and calculated results reported in [8].
Also, there is a low intensity mode observed at $\sim 268\ cm^{-1}$. This vibration can be attributed to the transverse optical (TO) Ga‑As phonon mode forbidden by the selection rules for Raman scattering. This mode can appear in the Raman spectrum due to the violation of symmetry in the sample because of some structural disorder induced by the incorporation of chromium [9].
It is clearly appreciated that the LO corresponding peak is asymmetric, more marked for the greater frequency side. This asymmetry is the result of other vibrational modes manifesting that will be studied forward, such as the longitudinal from the Cr-As and Cr-Ga vibrations (~ 321 and $\sim 336\ cm^{-1}$, respectively [9]), and those resulting from the coupling between LO phonons with the collective oscillations of the free carrier system (plasmons).
The superposition of all of them produces the observed effect. The difference between the two surfaces in this region can be caused by, among another probable causes, to the inhomogeneity of the Cr distribution inside the GaAs virgin material, which is incorporated into the sample by deposition on the surface and posterior thermal diffusion.

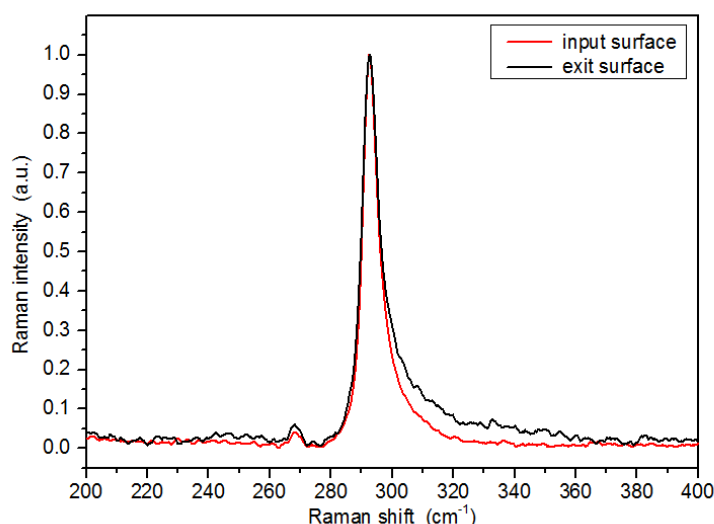

Figure 13. Comparison of Raman Spectra on the two surfaces of the sample before irradiation.

It is also appreciated that at low frequencies, especially at regions between 220 and 275 cm^{-1} there is an increase of the intensity of the background signal that can be a result of the presence of vibrational modes related to the existence of arsenic precipitates (clusters) on the sample resulting of the crystal synthesis process (broad Raman peak between 160 and 260 cm-1) [10]; but also on this region is observable a broad feature due to the photon density of states of GaAs or additional amorphous structures with specific medium range ordering [11]. Overtone and combination phonon modes of GaAs also appear in this spectral range [12].

Figures 14 and 15 show the measured spectra on both sides of the detector before and after irradiation. They are presented by superposition for each surface so that for each surface the effect produced by the 20 MeV electrons can be observed. Table 2 shows a summary of the most important peaks on the spectra and their respective intensities determined by different methods enabled on the ORIGIN v.9 code system.

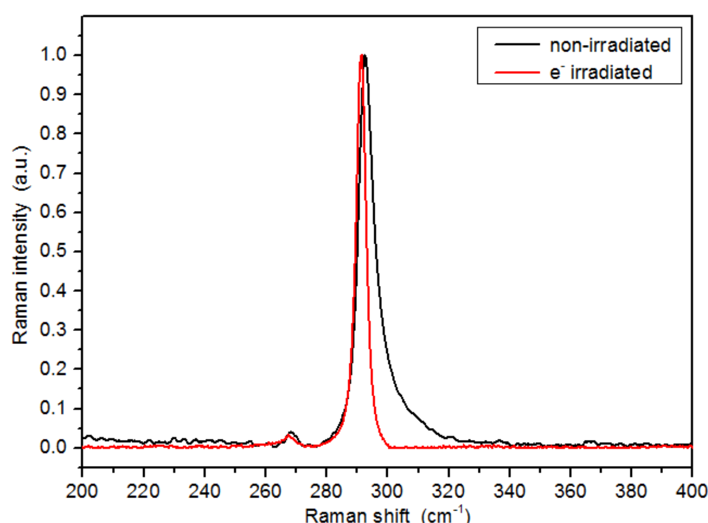

Figure 14. Comparison of Raman spectra on the input surface before and after irradiation.

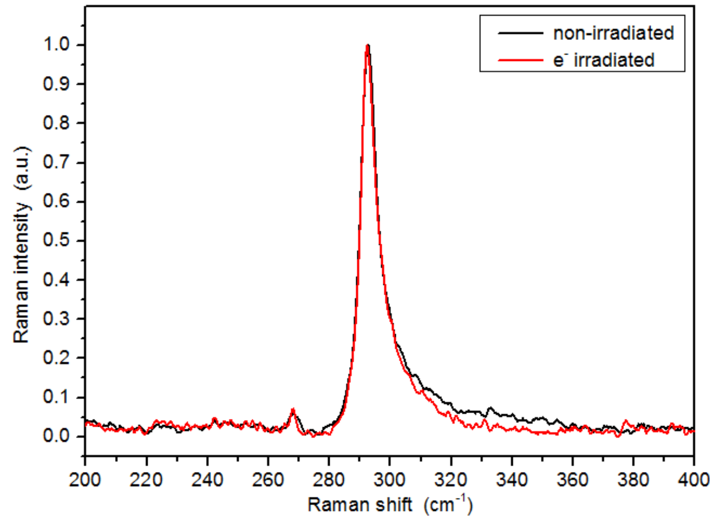

Figure 15. Comparison of Raman spectra measured on the exit surface before and after irradiation.

Figure 14 shows the side of the detector where the electrons impacted, which turned out to be where the most significant changes occurred, observing variations both on the shape of the peaks from the most representative optical modes and their shifts towards the low frequencies.

These shifts are not very significant ($\sim 1\ cm^{-1}$,), but they indicate that phenomena stimulated by irradiation may be occurring modifying slightly the tensional state of the structure.

Table 2. Principal characteristics of most relevant peaks observed on figure 14 and 15 spectra determined by different methods.

	Raman shift (cm^-1)		Intensity (a.u.)	
	LO mode	TO mode	LO mode	TO mode
Non-irradiated				
Input surface				
By Peak Analyze	292.40	268.24	1	0.04095
By Lorentz Fit	292.69 (3)	268.45 (6)		
By Gaussian Fit	292.70 (3)	268.45 (6)		
Exit surface				
By Peak Analyze	292.82	268.24	1	0.02525
By Lorentz Fit	292.79 (4)	268.24 (8)		
By Gaussian Fit	292.82 (4)	268.27 (6)		
Irradiated				
Input surface				
By Peak Analyze	291.51	267.31	1	0.03271
By Lorentz Fit	291.20 (1)	267.47 (6)		
By Gaussian Fit	291.21 (1)	267.47 (9)		
Exit surface				
By Peak Analyze	292.36	268.16	1	0.07108
By Lorentz Fit	292.70 (6)	267.95 (1)		
By Gaussian Fit	292.70 (5)	267.95 (1)		

At low frequencies after irradiation the broad feature stops being noticed practically completely.

In contrast, figure 13 shows how the effect of the radiation with electrons of 20 MeV is much less marked on the output side, or opposite to the incidence.
After exposure, the spectrum corresponding to the output side changes slightly only on the region of the high frequencies of the most intense peak (LO). However, the position and intensities ratio of the TO and LO modes are not affected.
Next, will be analyzed in more detail the spectrum region of greater interest, between 265 and $320\ cm^{-1}$, for which we will proceed to deconvolve the spectra in their Gaussian contributions, evaluate and compare the characteristics of these before and after of irradiation.

Analysis of the measured Raman spectra.

The processing of the spectra was done using the codes systems ORIGIN v.9 [13] and Peak Fit v.4.12 [14].
The spectra deconvolutions were made using the Lorentz, Gaussian and some variants of Voigt functions, but the best results were obtained only employing the Gaussian functions, and they are the results that will be presented below.
Figure 16 shows the spectrum structure in the range of interest for the input sample surface before irradiation.
Optical modes TO and LO are easily identified because they appear in the expected reported in the literature frequencies, as explained before. The presence of a peak with very low intensity in the position coinciding with those of the surface optical mode (SO) in GaAs is also seen.
A fourth mode is identified very close to the LO mode with an appreciable intensity, lower than LO, but with greater full width at half maximum (FWMH).This must be the resulting positive branch of the electrostatic coupling of longitudinal optical phonons with the surrounding charge carriers (carrier plasmons) result in the formation of LO phonon-plasmon modes (or LO phonon-plasmon coupled (LOPC)), also called plasmarons, which can mediate the carrier lattice energy exchange and thus play an important role in the electrical characteristics of semiconductor-based devices [15].

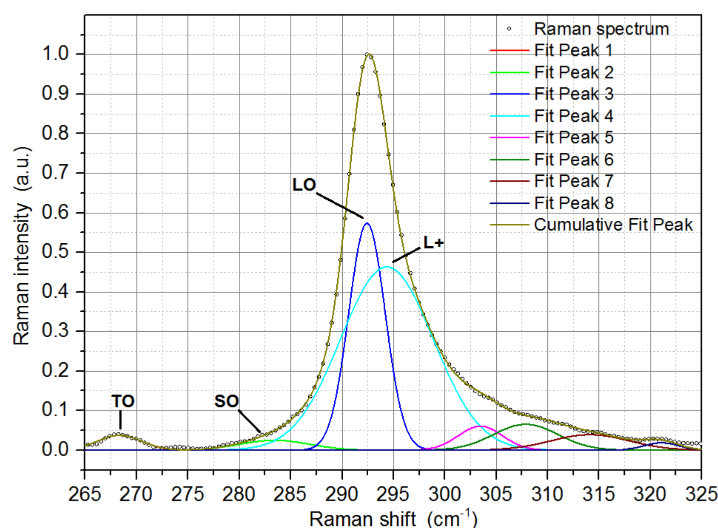

Figure 16. Deconvolution of the Raman spectrum of target sample's input surface before the electron irradiation.

In polar semiconductors LO phonons couple strongly with the collective oscillations of the free-carrier system (plasmons). The extent of coupling, or mixing, is greatest when the two modes are of comparable energies and depends strongly on carrier concentration. For n-GaAs this results in two LOPC branches, L+ (upper) and L- (lower), for a given plasma frequency, but due to large carrier damping, only one LOPC mode is generally observed in p-GaAs [16].
The mode that appears at the frequency of $294.35\ cm^{-1}$ can be identified as the LOPC L+. This is in correspondence with the reports of the literature concerning that in environmental conditions the TO and L- modes may occur close to each other depending on the free electron concentration and wave length of the laser. In this situation, it is possible that it takes place and overlapping between L- and TO peaks, being impossible to solve both peaks, as it happens in our case [17].
Finally, above $300\ cm^{-1}$ the presence of several Gaussian peaks is observed which give rise to a very broad feature. These peaks have not been completely clarified and their study continues.
It is important to note that these presumed modes together with the LOPC could be thought to be a single very broad mode that results from the interaction of longitudinal optical phonon with the free carriers of the material and this would explain the behavior observed after irradiation (see below). However, a mathematical adjustment of this unique broad feature through a single curve was impossible.
The deconvoluted Raman spectra of the sample's input surface after de irradiation process is shown in figure 17.

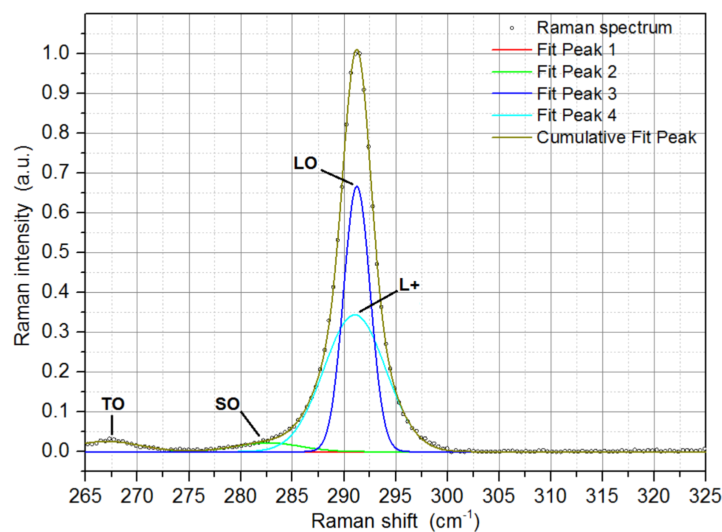

Figure 17. Deconvolution of the Raman spectra of target sample's input surface after the electron irradiation.

The most relevant thing that is observed is the almost total "disappearance" of the broad feature that previously appeared for frequencies higher than $300\ cm^{-1}$. As mentioned above, in this sense the work continues.
However, it is very important that although TO and SO have slightly moved towards low frequencies (0.53 and $0.82\ cm^{-1}$ respectively), LO mode shifted to red $1.38 cm^{-1}$and L+ shifted $3.11\ cm^{-1}$.
As already mentioned, the red shift of the fundamental optical modes can be linked to a certain relaxation of the stress present in the structure, which at the doses used is not very significant. But in the case of L+ this strong shift is the result of a decrease in the concentration of free carrier in the sample [17], a process stimulated by radiation.

Figures 18 and 19 show the deconvolved Raman spectra for the exit surface, before and after the exposition to the electron flow from the accelerator.

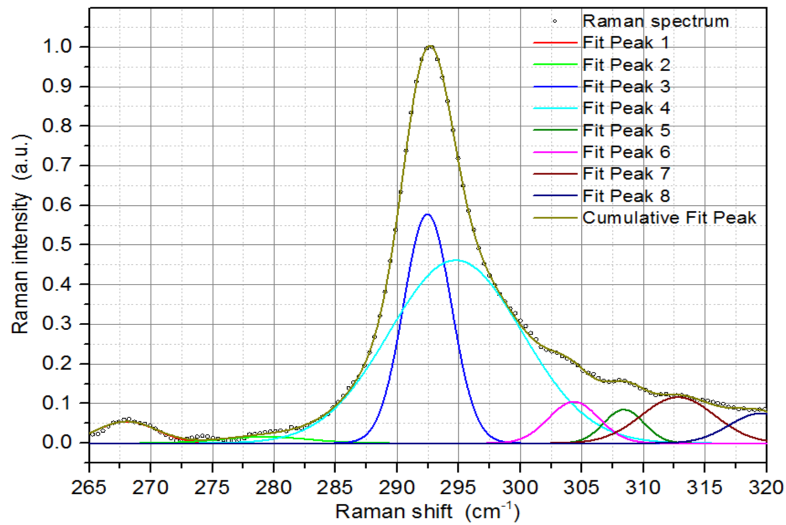

Figure 18. Deconvolution of the Raman spectrum of target sample's exit surface before the electron irradiation.

Contrasting what happens with the incidence surface, here the post-irradiation changes are much less significant.

Before and after irradiation, the presence of the same peaks obtained for the deconvoluted spectrum of the incidence non-irradiated surface is observed (in the figures the peaks are not identified with letters, but the same colors for the lines are used).

Comparing both spectra (figures 17 and 18), it can be observed that the positions of the modes remain practically unchanged ($\Delta<0.2\ cm^{-1}$), but the intensities and widths of some peaks changed noticeably.

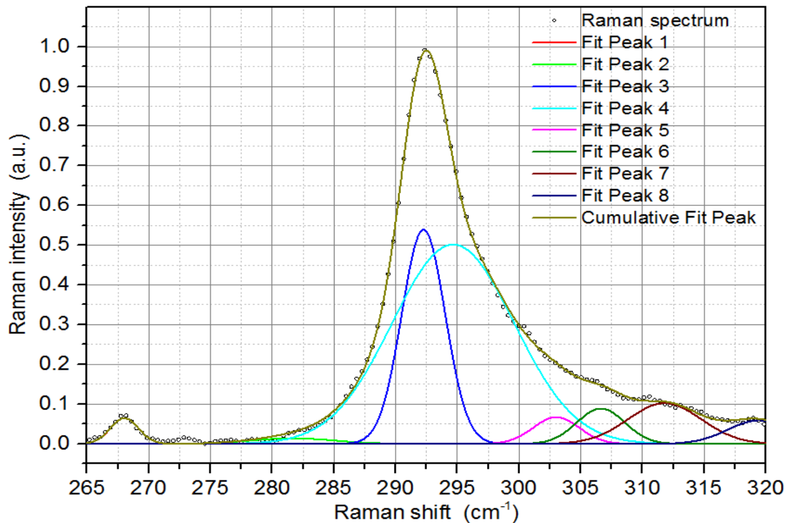

Figure 19. Deconvolution of the Raman spectrum of target sample's exit surface after the electron irradiation.

It is noteworthy the change in the LO/L+ intensity ratio that may be a consequence of the slight increase in the coupling between LO and the plasmons of the target. The corresponding peak and TO narrows and intensifies.

These spectra are still being studied and new experiments are planned to verify the behaviors that are observed now and to clarify the unknowns that still exist. It is advisable to use new detectors of higher quality.
It is also planned in the immediate future to try to perform the fitting of the broad feature observed in the right region of the highest mode in the Raman spectra using the Lindhard–Mermin function, as reported in [18].

Acknowledgements.

I want to thank the JINR, and in particular the Organizing Committee of the SSP'2018, for giving me the great opportunity to participate in this program and for all the attention they have given to me during my stay.
I want to specially thank my supervisor, Prof. Dr. Antonio Leyva Fabelo for his constant advice, his valuable and constructive suggestions during the development of this work, his patient guidance and for providing me all the things I’ve learned from him during this program.
Also, I would like to acknowledge Prof. Dr. Alexei Zhemchugov, Dr. Said Shakur and Dr. Uladzimir Kruchonak for their support and assistance that has been a great help to develop this research.
My special thanks are extended to the colleagues from DLNP, a collective that during the period of work assimilated me as another collaborator of the Laboratory.
Finally, I wish to thank all the scientists from the laboratories we visited during the SSP’2018 for enabling me to visit their offices to observe their interesting daily operations.

References.

1. Gersch H. K., McGregor D. S. and Simpson P. A. NIM A 489, (2002), 85-98.
2. Ferraro J. R., Nakamoto K. and Brown Ch. W. Introductory Raman Spectroscopy. Elsevier Inc., Academic Press, 2nd edition, (2003).
3. ImageJ - https://imagej.nih.gov/ij/
4. Photoshop - www.photoshop.com
5. Matlab - https://la.mathworks.com/products/matlab.html
6. Jellison G.E. Optical Materials 1(3) (1992) 151-160.
7. Piñera I., Cruz C. M., Leyva A., et al. NIM B 339 (2014) 1-7.
8. Harrison W. A. Electronic structure and the properties of solids, W. H. Freeman and Company, San Francisco, (1980).
9. Seredin P. V., Fedyukin A. V., Arsentyev I. N., et al., Semiconductors 50(7) (2016) 853-859.
10. Jiang D. S., X. P. Li, B. Q. Sun et al. J. Phys. D: Appl. Phys. 32 (1999) 629-631.
11. Mishra S., Kabiraj D., Roy A. and Ghosh S. Sol. Stat. Comm. 150 (2010) 1892-1895.
12. Mishra S., Kabiraj D., Roy A. and Ghosh S. J. Raman Spectrosc. 43 (2012) 344-350.
13. Origin - www.OriginLab.com
14. PeakFit - http://www.sigmaplot.co.uk/products/peakfit/peakfit.php
15. Rocca M. 9.4 Plasmon-Phonon coupling in semiconductor. In: Chiarotti G., Chiaradia P. (eds) Physics of Solid Surfaces. Landolt-Börnstein - Group III Condensed Matter vol. 45A. Springer, Berlin, Heidelberg, (2015).
16. Fukasawa R. and Perkowitz S. Phys. Rev. B 50(19) (1994)14119.
17. Varandani D., Dilawar N., Chakraborty B. R., et al. J. Mat. Sc. Lett. 20 (2001) 5–7.
18. G. Abstreiter, M. Cardona, and A. Pinczuk. Light Scttering in Solids IV, Topics in Applied Physics vol. 54. Springer Verlag, Berlin, 1984.